Diamond & Related Materials 132 (2023) 109648

Contents lists available at ScienceDirect

Diamond & Related Materials

journal homepage: www.elsevier.com/locate/diamond

Investigation of transition metal-doped graphitic carbon nitride for MO dye degradation

Asif Hussain [a,b,c], Samayya Maqsood [c], Renlong Ji [d], Qikai Zhang [e], M. Umer Farooq [f], M. Boota [c], M. Umer [c], M. Hashim [c], Hamza Naeem [f], Zaigham Saeed Toor [g], Asghar Ali [c], Jianhua Hou [a,b,*], Yuxiong Xue [h,*], Xiaozhi Wang [a,b,*]

[a] College of Environmental Science and Engineering, Yangzhou University, Yangzhou 225127, People's Republic of China
[b] College of Physical Science and Technology, Yangzhou University, Yangzhou 225127, People's Republic of China
[c] Department of Physics, University of Lahore, Lahore, Pakistan
[d] College of Materials Science and Engineering, Yantai Nanshan University, No.12, Daxue Road, Donghai Tourist Resort, Longkou City in Shandong Province 265713, People's Republic of China
[e] Beijing Xinfeng Aerospace Equipment Co., Ltd, Beijing, 100854
[f] Department of Physics Division of Science and Technology, University of Education Lahore, Pakistan
[g] Department of material Science and Engineering, Institute of Space Technology, Islamabad, Pakistan
[h] College of Electrical, Energy and Power Engineering, Yangzhou University, Yangzhou 225127, People's Republic of China

ARTICLE INFO

Keywords:
Photo-catalysis
Degradation
Methyl Orange (MO)
g-C_3N_4
Visible light

ABSTRACT

Graphitic carbon nitride (g-C_3N_4) has received significant attention recently as a metal-free and visible-light responsive photo-catalyst because of its exceptional photocatalytic activity. The separation and transit efficiency of the photo-generated charge carriers determines the photocatalytic effectiveness of g-C_3N_4 and g-C_3N_4-based materials for contaminant degradation. Therefore, pure g-C_3N_4 typically shows low impact. Herein, metal-doped (Copper (Cu), Manganese (Mn), and Zinc (Zn)) g-C_3N_4 is synthesized by an easy high-temperature process to enhance the performance of g-C_3N_4. The XRD, SEM, UV–vis DRS, measurements, photocatalytic testing, etc. are used to describe and evaluate the synthesized materials. As a result, metal-doped photo-catalysts exemplified improved visible-light photocatalytic activities for pollutants degradation with the benefits of reduced band gaps for prolonged visible-light absorption, and improved electronic structures for effective charge transfer. The Zn-doped g-C_3N_4 in particular exhibited efficient use of photo-generated electron-hole charge carriers during the pollutant degradation process due to the excellent tailoring, including both electronic structure and microstructures. As a result, the Zn-doped g-C_3N_4 photo-catalyst exhibits the highest photocatalytic performance for Methyl Blue (MO) dye degradation. During the degradation process of the samples, i.e. (g-C_3N_4, Cu-g-C_3N_4, Mn-g-C_3N_4, and Zn-g-C_3N_4) the MO degradation rate is achieved, such as 40 %, 60 %, 80 %, and 90 %, respectively. Additionally, the main areas of investigation are the photo-degradation of MO dye and the photo-catalytic mechanism.

1. Introduction

The use of semiconductor photo-catalysts to convert solar energy into sustainable fuels and chemicals has been a widely used technique in the development of sustainable and environmental cleanup [1–3]. Over the years, various semiconductors such as sulphides, oxides, and nitrides, have been studied as active photo-catalysts [4–6]. Therefore, the low efficiency of pollutant degradation for photo-catalysis is the main obstacle to its widespread practical usage. Synthesizing extremely effective photocatalytic materials that can initiate higher degradation in the environment is one potential remedy [7].

In recent decades, the n-type polymer semiconductor g-C_3N_4 (graphitic carbon nitride) has attracted significant consideration owing to its band gap of around 2.7 eV [8,9], which permits visible absorption, and the specific redox ability for photo-induced charge carriers in the material's structures makes it potentially desirable for photocatalytic activity [10,11], which can be extensively exercised in water splitting, organic photosynthesis, and pollutant degradation [12,13]. It can be

* Corresponding authors at: School of Environmental Science and Engineering, Yangzhou University, Yangzhou 225127, People's Republic of China.
E-mail addresses: jhhou@yzu.edu.cn (J. Hou), 007436@yzu.edu.cn (Y. Xue), xzwang@yzu.edu.cn (X. Wang).

https://doi.org/10.1016/j.diamond.2022.109648
Received 21 October 2022; Received in revised form 13 December 2022; Accepted 19 December 2022
Available online 23 December 2022

used as a photo-catalyst for carbon-based synthesis [14], a photo-electric converter [15], an electrode material for batteries and fuel cells [16], a hydrogen storage material [17], and even as a fluorescent sensor [18]. However, fast recombination of photo-generated electron-hole pairs and the less surface area of g-C_3N_4 suppressed their efficiency [19]. Thus, several efforts have been made to resolve these drawbacks, e. g. doping with heteroatoms [20], tuning compositions [21], coupling with other semiconductors [22], and preparation of nano or porous g-C_3N_4 [22]. Another effective remedy is through the fabrication of a material at the nanoscale to minimize the defects in crystals in order to avoid an increase in carrier recombination [23,24]. The size, morphology, shape, surface area, and dimension of nanostructures are essential characteristics for photocatalytic activities [25].

Furthermore, metal-doping is an effective mechanism for improving photo-catalytic properties of semiconductors and has assisted in a significant interest in regulating optical bandgap and reducing in photo-generated electron hole recombination [24,26]. In order to generate a charge polarity variation with encouraged electron transfer while a non-radical process was reported by Guan et al. with Fe-doped to g-C_3N_4 microstructures [27]. Asymmetrically incorporating metallic Ni into the NiO matrix, Zhao et al. improved a non-radical efficiency by producing additional sites with oxygen vacancies [28]. According to Wei et al., the presence of iodine vacancies may both lower the Bi valence and raise the carrier density, which will boost the catalyst's ability to transfer electrons to peroxydisulfate and accept electrons from the organic matrix [29]. According to Zuo et al., the CuO-CN polarization electric field had an imbalanced charge distribution, which increased the absence of charge on the CuO's outer surface and promoted non-radical activation [30]. It has been demonstrated that with just these two techniques, the catalyst's electronic structure can be changed to improve catalytic performance.

In this study, metal-doped (Cu, Mn, and Zn) g-C_3N_4 nano-structures were prepared with a facile synthesis method. A simple solid-state reaction technique is used to synthesized, which is easily available and accessible or may be commercialized. The water-soluble organic synthetic dye methyl orange (MO) was employed as an organic pollutant. Here, we used Carbamide (CH_4N_2O) as a base material for g-C_3N_4 synthesis and metal salts like Cu, Mn, and Zn as dopant, which regulated optical bandgap lower and upper states, enhanced optical absorption, and altered structural morphologies, resulting in higher photocatalytic efficiency is attained.

2. Experimental section

2.1. Materials

Urea (CH_4N_2O), Copper Chloride ($CuCl_2$), Magnesium Chloride ($MnCl_2$), and Zinc Chloride ($ZnCl_2$) were purchased from Sinopharm Chemical Reagent Co., Ltd. (Shanghai, China). The organic compound Methyl Orange (MO), isopropyl alcohol (IPA), distilled water, P-benzoquinone (BQ), Edta disodium (EDTA-2Na) were purchased from Sinopharm Chemical Reagent Co, Ltd. (Shanghai, China). All materials were consumed without further modification.

2.2. Synthesis of g-C_3N_4

The g-C_3N_4 (graphitic carbon nitride) is synthesized urea using the thermal decomposition process. The 10 g urea is placed in a crucible, put in a muffle furnace for 2 h, heated to 550 °C at a rate of 5.0 °C per min for 2 h in an open environment, the furnace's 550 °C temperature was sustained for 2 h before it cooled to room temperature. Using a mortar and pestle to crush the acquired yellowish material (g-C_3N_4), additional processing was performed to produce a fine powder.

2.3. Synthesis of metal-doped g-C_3N_4

The Copper Chloride ($CuCl_2$) modified g-C_3N_4 was prepared using Urea (5 g of urea (99.9 % pure)) along with 0.15 g of Copper Chloride ($CuCl_2$) (3 % doping factor). Both materials were crushed into powder form until they reached a homogenous mixture. The powder was then placed in a muffle furnace using an alumina crucible at 550 °C for at least 2 h. After cooling down to room temperature, copper modified g-C_3N_4 structures were collected and denoted as Cu-g-C_3N_4. The same procedure was adopted for the synthesis of Mn-g-C_3N_4 and Zn-g-C_3N_4.

The Manganese Chloride ($MnCl_2$) and Zinc Chloride ($ZnCl_2$) modified g-C_3N_4 were synthesized using the same procedure mentioned above, and the collected samples were named as Mn-g-C_3N_4 and Zn-g-C_3N_4.

2.4. Characterization

X-ray Diffraction (XRD) (Philips X' Pert Pro MPD) is used to analyze the crystal structures of all the synthesized materials. Scanning electron microscopy (Hitachi S-4800) is used to examine the microstructure of the fabricated samples. Methyl-Orange (MO) dye degradation was used to evaluate the products' stability and effectiveness. In order to examine, band gaps and K values, UV–Vis. spectra were recorded. All samples' bandgaps and K values were calculated from these measurements, as shown in Figs. 3 and 5.

3. Result and discussion

3.1. Structural and compositional analysis

In order to investigate the crystal structure of the pristine and transition metal-doped (Cu, Mn, and Zn) g-C_3N_4. All the samples were tested using X-ray diffraction. Fig. 2 displays the recorded diffraction patterns (θ-2θ scans) for each sample. Two diffraction peaks recorded for the pristine g-C_3N_4 can be observed at diffraction angles of 13.1° and 27.3°, respectively. These reflections correspond to the (100) and (002) planes of the g-C_3N_4. The observed diffraction peaks measured for the synthesized g-C_3N_4 are well matched with the graphitic structure of g-C_3N_4 (JCPDS: 87-1526). The diffraction peak appeared at a diffraction angle of 13.1°, which represented the unit of tri-*s*-triazine connecting to trigonal nitrogen. The aromatic conjugated structures for long range interplanar stacking are demonstrated by the strongest peak that appeared at diffraction angle 27.3° [31]. It can also be observed that the diffraction peaks recorded for the (002) plane of the metal-doped g-C_3N_4 have a lower intensity as compared to the un-doped sample. Additionally, the diffraction peak representing metal-doped g-C_3N_4 samples is shifted toward a lower diffraction angle compared to pure g-C_3N_4. Moreover, the diffraction peaks representing the doped samples are significantly broader compared to un-doped samples. The reduction in peak intensity can be attributed to the thinning nature of doped g-C_3N_4 successive layers as compared to pure g-C_3N_4. The broadening of the diffraction peaks may be attributed to the presence of the strain in the layered structure caused by the doping as commonly reported in the literature. While the peak shift toward the lower diffraction angle can be attributed to an increase in the interatomic spacing, therefore increasing the distance between successive layers of the doped g-C_3N_4 accordingly.

In order to investigate the microstructure and surface morphology of the synthesized un-doped and transition metal-doped (Cu, Mn, and Zn) g-C_3N_4 samples, Scanning Electron Microscopy (SEM) images were recorded. The SEM images of all the samples are shown in Fig. 3. The SEM micrograph displayed in the Fig. 3(a) shows that the synthesized g-C_3N_4 is consists of round shaped grains. The non-uniform size distribution of the grains in the images may be attributed to the sticking of the grains with each other. The SEM images recorded for this sample also give the impression of the presence of pores in the grains, which may be clearly seen using high resolution SEM images. The SEM images

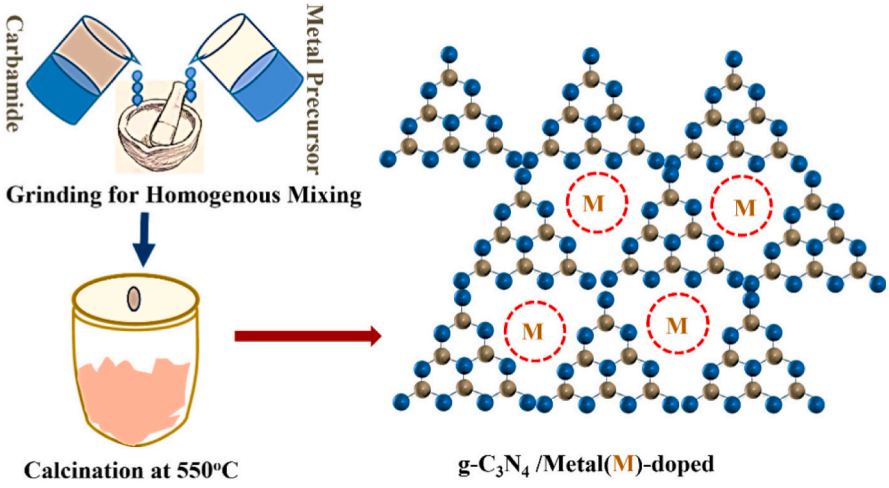

Fig. 1. Schematic diagrams of pure g-C_3N_4 and transition metal doped (Cu, Mn, and Zn) g-C_3N_4 structures.

obtained from the manganese doped g-C_3N_4 sample are shown in Fig. 3 (c). The microstructure of this sample looks different compared to the microstructure observed for the undoped g-C_3N_4 sample in terms of size and distribution of the grains. Additionally, SEM image representing Mn-g-C_3N_4 showed that the fabricated material has a fiber like surface, which is reported quite to be beneficial in photo-catalysis. The fibrous morphology of the material will show greater reactivity and longer stability. Fig. 3(b) represents the SEM images of the copper-doped g-C_3N_4 sample.

The microstructure of this sample is different compared to the observed microstructure of the un-doped and Mn-g-C_3N_4 sample. One difference that can be noticed is the size of the grains. It can be noticed that the size of the grains is bigger as compared to the undoped g-C_3N_4. Moreover, the grains have a non-uniform size distribution and are irregular in shape, with a larger surface area. The grains of a few micrometers in size can be observed at the bottom of the image, representing the Cu-g-C_3N_4. Fig. 3(d) displays the SEM images of the Zinc-doped g-C_3N_4 sample. A unique microstructure was observed for this sample. This sample exhibits an elongated flake-like microstructure. The images recorded at high resolution showed in the insect of the image indicate the existence of the pores inside the elongated flake like structures.

Based on a visual comparison, it was observed that for doped g-C_3N_4, not only a diverse and exhaustive modification of the morphology was achieved. In accordance with the different metal dopants added, but also the fiber or irregular shaped structures provided better surface area to volume ratios, thereby enhancing reactivity and photocatalytic effect accordingly.

4. UV–Vis analysis

According to Fig. 4, UV–Vis diffuse reflectance spectra was exercised to determine the optical bandgap energy for transitional metal-doped and pristine metal-free g-C_3N_4 semiconductors. Manganese and Zinc-doped g-C_3N_4 structures showed enhanced absorption corresponding to the pristine. As a result, it would encourage higher solar energy and higher catalytic activity [32]. The mathematical formula listed below is exercised to ascertain the semiconductor bandgap potential energy (eV).

$$(\alpha h\nu)^n = A\left(h\nu - E_g\right) \tag{1}$$

The following symbols stand for the absorption coefficient, energy bandgap, Planck's constant, frequency, and band tailing constant, respectively: α, E_g, h, v, and A. where $n\ \left(2, and\ \frac{1}{2}\right)$ is a power factor of the transition mode indicating the nature of the material. For direct bandgap material, its value is 2, whereas in the case of indirect transition represented by representing $\frac{1}{2}$. The g-C_3N_4 bandgap potential energy is approximately 2.79 eV, while Cu-g-C_3N_4, Mn-g-C_3N_4, and Zn-g-C_3N_4 have bandgap energies are 2.70 eV, 2.56 eV, and 2.49 eV, respectively. Therefore, enhanced solar energy absorption is accredited to narrow bandgap energy. Resulting, in higher photocatalytic efficiency, as shown in Figs. 4 and 5. The expressions shown below are exercised to evaluate the conduction band minimum energy (E_{CB}) positions and the valence band maximum energy (E_{VB}) positions [33].

$$E_{CB} = \chi - E_e - 0.5E_g \tag{2}$$

$$E_{VB} = E_{CB} + E_g \tag{3}$$

here, E_{CB} and E_{VB} signified conduction band (higher energy state) and valance band (lower energy state) energy, χ, E_g and E_e indicated absolute electronegativity (Mulliken), bandgap energy, and free electron energy (4.50 eV) on the hydrogen scale.

It is recognized that g-C_3N_4 has an absolute electronegativity of precisely 4.67 eV. The valence band edges have are at 1.63 eV, 1.58 eV, 1.51 eV, and 1.50 eV potential energies, respectively, as shown in Fig. 4b, which is shifted toward lower potential. The conduction band edges are at 1.17 eV, 1.05 eV, and 0.97 eV, potential energies, respectively, corresponding to the g-C_3N_4, P-g-C_3N_4, and S-g-C_3N_4 structures, which is explained by the valence band and conduction band locations, as well as possibly the induction of substates within the band structure of g-C_3N_4, which were modified by the transition-metals doping. Additionally, compared to the pristine g-C_3N_4 allowing a bandgap of 2.80 eV, the bandgap significantly fell to 0.4 eV. This is explained by the fact that nonmetal doping caused the narrow bandgap.

5. Photocatalytic activity

The Methyl Orange (MO) dye was exercised to evaluate the g-C_3N_4 photocatalytic activity and metal-doped g-C_3N_4 composite performance, as shown in Fig. 3a. It can be shown from absorption spectra that the breakdown of MO dye undergoes significant modifications. A photo-degradation reaction results in a positive doping finding. Fig. 6a describes the MO dye degradation using pure g-C_3N_4, whose degrading photocatalytic activity was noticeably low, leading to it taking 150 min for the 60 % degradation to be completed. The absorption intensity of MO dye is decreases slowly. Even after 150 mins, 60 % of the dye degrades, resulting in higher photo-generated electrons-holes recombination and low absorption of solar energy, which is attributed to lower photocatalytic activity [34]. As compared to bulk g-C_3N_4, the Cu-doped

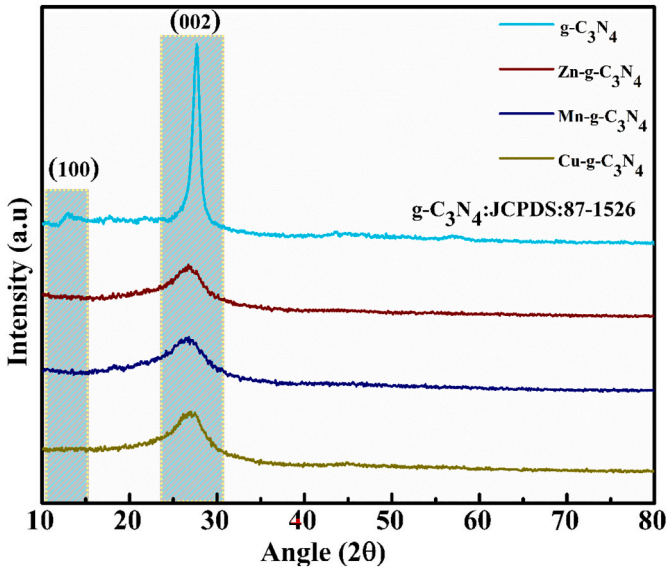

Fig. 2. XRD diffraction pattern for the bulk g-C_3N_4 and metal-doped g-C_3N_4.

g-C_3N_4 composite confirmed improved photocatalytic activity as shown in Fig. 3b. which could be justified by the fact that the extra mass of Cu could offer more catalytic sites, allowing for more •OH to be produced as a result of the interactions between Cu and H_2O_2 [35]. However, the pollutants' degradation performance may be increased or decreased based on the Cu mass concentration [35]. As visible energy is irradiated, the photocatalytic efficiency of the Mn-doped g-C_3N_4 composites exhibits a considerable variation for MO dye degradation, as viewed in Fig. 3c. The higher concentration of Mn was considered to have higher catalytic sites but did not have a significant photocatalytic performance because the tri-*s*-triazine structure was damaged and there was a speedy reduction in specific surface area as shown in Fig. 1 [36]. The structures of and catalytic activity of g-C_3N_4 can be damaged by heavy cobalt doping, according to previous study. During the potential-catalytic preparation, as shown in Fig. 3d, zinc was significantly influenced, with a longer absorption edge and higher light absorption intensity. As a result, higher degradation was attained by the Zn-g-C_3N_4 sample as compared to the g-C_3N_4, Cu-g-C_3N_4, and Mn-g-C_3N_4. The catalytic activity of MO dye was monitored with pristine g-C_3N_4 and transitional metal-doped (Cu, Mn, and Zn elements) using solar energy irradiation as shown in Figs. 3 and 4. Typically, the Langmuir-Hinshelwood model is used to investigate how organic pollutants degrade when exposed to solar energy irradiation. Additionally, it is considered that the photocatalytic interaction occurs between the molecules of absorbed contaminants and the photogenerated active species. For the breakdown of pollutants, first-order kinetics is hence efficient and straightforward [9]. Therefore, Fig. 4b, c shows the photodegradation reaction constant (k) for g-C_3N_4 and doped elements, namely Cu, Mn, and Zn. The first-order kinetic reaction is represented by the mathematical expression as mentioned in Eq. (1).

$$ln\left(\frac{C_0}{C}\right) = Kt \tag{4}$$

here, initial concentration, verified concentration, kinetic constant, and reaction time are denoted by C_0, C, K, and t, respectively. The synthesized samples such as g-C_3N_4, Cu-g-C_3N_4, and Mn-g-C_3N_4, and Zn-g-C_3N_4 and their respective significant values of K were tested, 5.71×10^{-2}, 7.27×10^{-2}, 8.51×10^{-2}, and 9.50×10^{-2}, respectively. Based on results and experiments, it is possible to conclude that among the transitional metals Zn doped g-C_3N_4 sample has a higher pollutant degradation efficiency of approximately 81 %. Moreover, it is also being investigated whether a metal-doped strategy can enhance catalytic activity. However, higher metal contents are more active and react quickly with surrounding reactants to produce undesirable species, which causes photocatalyst stability to be less than satisfactory [37].

A graph was made between C/C_0 and time (mins) to further clarify the photocatalytic performance of the materials created based on solar

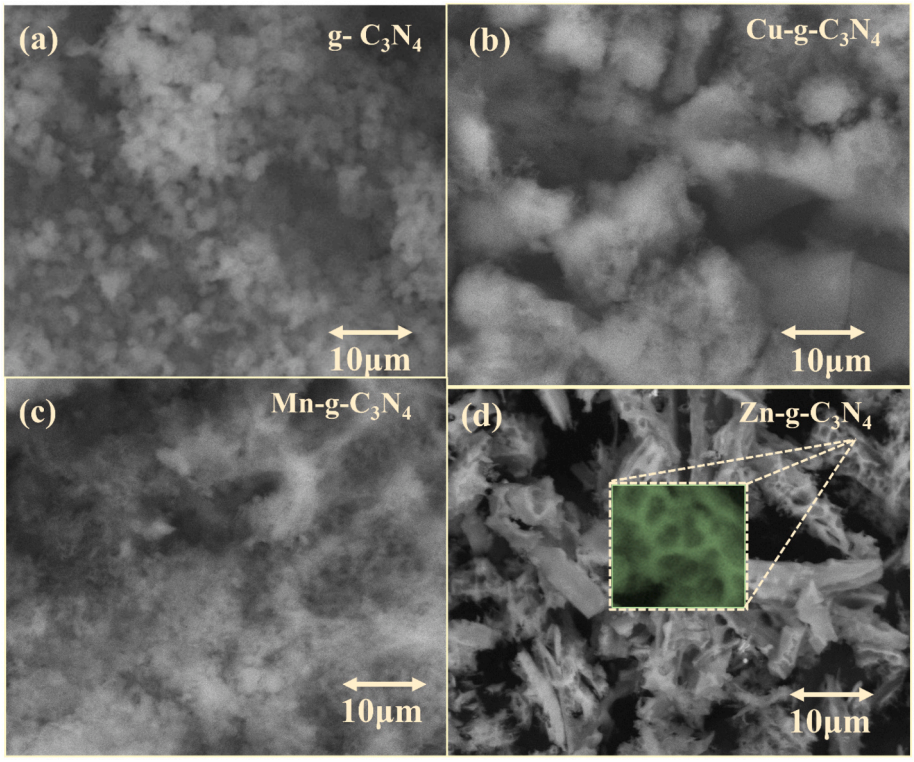

Fig. 3. SEM Images of (a) bulk g-C_3N_4, (b) Cu-g-C_3N_4, (c) Mn-g-C_3N_4, (d) Zn-g-C_3N_4.

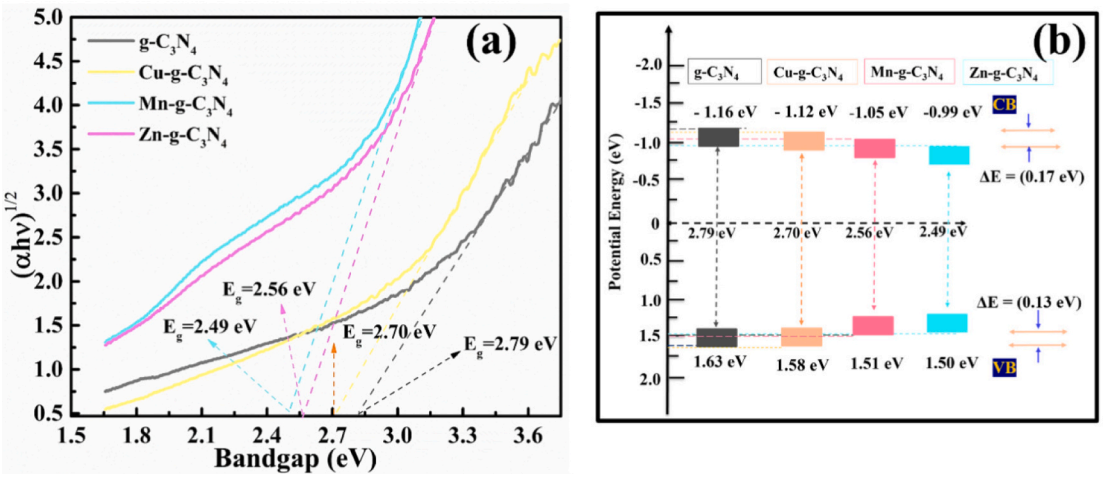

Fig. 4. Transitional metal doped and pristine g-C_3N_4 elements bandgap energy (a), valance and conduction band potential energy potions (b).

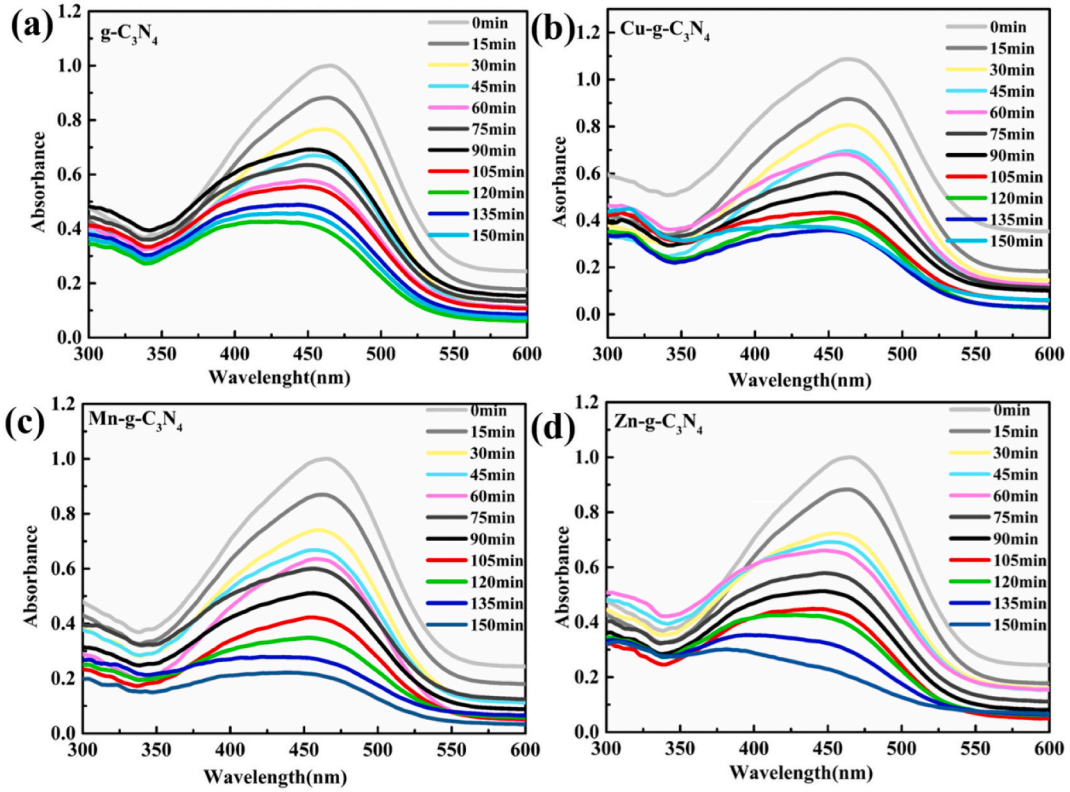

Fig. 5. Absorption Spectra for MO dye (a) g-C_3N_4, (b) Cu-g-C_3N_4, (c) Mn-g-C_3N_4, and (d) Zn-g-C_3N_4 samples.

energy irradiation spectrum. C/C_0 describes the intensity of the MO dye at a specified time. The authors observed that Zn and Mn showed better results of photocatalysis as compared to pure CGN according to the graph shown in Fig. 6. Initially, Zn showed a sudden decrease in the MO dye concentration as compared to Mn and pure g-C_3N_4 at time 30 min. But as time went on, the reactivity of the pure g-C_3N_4 decreased, but the Zn and Mn kept decomposing all the MO dye. At $t = 125$ mins, both Zn and Mn showed the same amount of concentration of MO dye, leading to the fact that Zinc, due to its better conductivity, is competing with Mn, but after this point, Zn still goes on to further decompose the dye, showing the best fabricated material from the other samples. This can be attributed to the fact that due to doping, the concentration of active species for first-order kinetic reaction becomes enhanced, which results in prolonged and rapid degradation of the dye in the presence of a catalyst.

The formula used to calculate the reactivity values is given below:

$$k\,t = C/C_0$$

Another form of this formula is:

$$k\,t = ln\left(\frac{C_0}{C}\right)$$

By rearranging the above formula, we calculated the value of 'k' which shows the reactivity of a photocatalyst, or commonly known as the photodegradation constant. From Fig. 7, we observed that pure g-C_3N_4 had a very low k value, which indicated that the reactivity of the

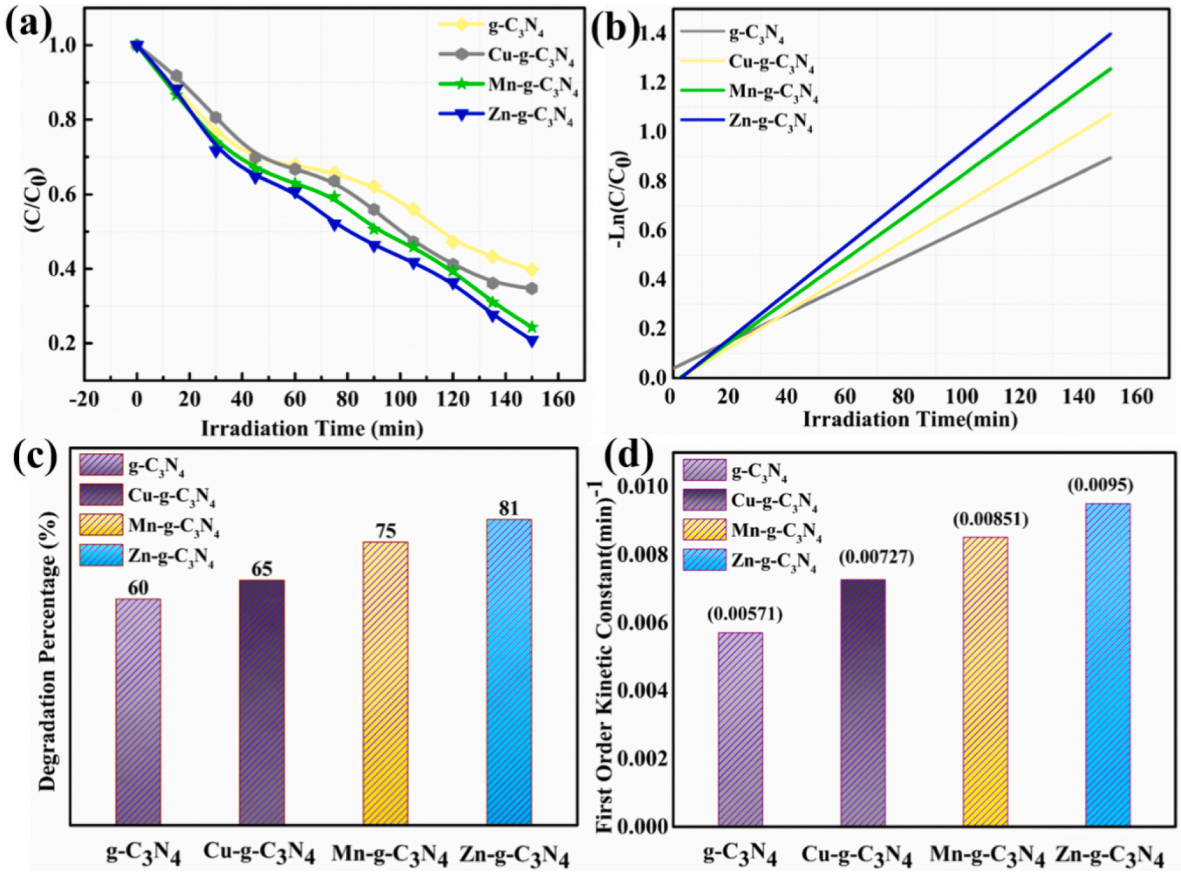

Fig. 6. Methyl orange photodegradation (a), $Ln\left(\frac{C_t}{C_0}\right)$ Vs 't' graph (b), percentage of photo-degradation (c), and kinetic constant 'K' for g-C_3N_4, Cu-g-C_3N_4, Mn-g-C_3N_4, and Zn-g-C_3N_4.

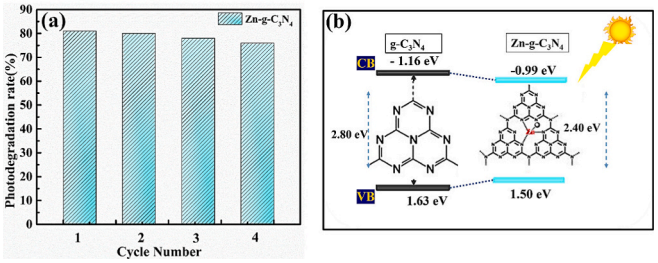

Fig. 7. Transition metal-doped g-C3N4 photocatalysts stability test (a), schematic diagram for photocatalytic mechanism.

sample was weak, leading to low degradation and taking more time. Whereas other samples showed a significant higher k value, exhibiting greater reactivity along with less degradation time.

6. Photocatalytic mechanism

Considering the aforementioned scientific examination and observations, the potential photocatalytic mechanism is explained. Corresponding to the results, pristine g-C_3N_4 exhibited decreased photocatalytic activity, which is accredited to higher electron-hole recombination, lower solar energy absorption, or possibly because the conduction band minima have a larger negative potential, which is approximately (−1.16 eV) as shown in Fig. 4b. The g-C3N4 nitrogen (N) atoms provide active sites which may take part in photocatalytic processes. The localized structure of g-C_3N_4 between the carbon atoms C and N confined electrons available around the N atoms and the transfer of excited electrons [38]. Additionally, the possibility of photo-generated electron-hole recombination may be increased by the back transition of excited electrons for redox reactions [33,39]. According to the DFT theory, doping produced an excited electron pathway from a N atom to a doped atom, which improved localized active sites, reduced charge recombination, and altered reaction properties [40]. Cu doping is attributed to a reduction in optical bandgap, enhanced reaction constant rate (5.7×10^{-3}-7.2×10^{-3}), which enhances visible energy absorption, resulting in increased catalytic activity. In addition, according to our conclusions, Cu species doped in g-C_3N_4 are capable of MO degrading pollutants, but satisfactory results are not yet realized. However, further research may be required to ascertain what role the Cu species of the Cu-doped carbon nitride play in the catalytic process cycle and how the complex interaction between the elements copper and carbon nitride affects the photocatalytic activity of the substance. Furthermore, we think that the Cu-doped catalyst's catalytic activity in building carbon nitride in ultrathin nanosheets could further improve the material by connecting it with conductive substrates (like graphene and carbon). The Mn doped g-C_3N_4 was verified for MO degradation, which exhibited improved catalytic activity corresponding to the pristine and Cu doped g-C_3N_4. Once solar energy irradiated across the Mn-g-C_3N_4 photocatalyst, electron-hole pairs generated and exited electrons from VB shifted toward CB of Mn-g-C_3N_4 generated a substate at CB lower sate, causing a lower CB edge potential energy (−1.05 eV), which is a shift toward the positive potential of g-C_3N_4 (−1.16 eV) [41,42]. The Zn doped catalyst displayed enhanced catalytic activity corresponding to the pristine, Cu, and Mn doped g-C_3N_4, a consequence of the narrow optical bandgap (about 2.49 eV), CB potential (−0.99 eV) and VB

potential (1.5 eV) confirmed the shifting of bandgap to higher potential as shown in Fig. 4b, which verified higher solar energy absorption. Moreover, spongy porous structures may have more surface area, which additionally promotes higher catalytic activity. The reusability and stability of a transitional metal-doped catalyst are two other practical considerations for catalyst research. A number of tests were conducted over Zn-g-C_3N_4 for the degradation of MO through the irradiation of solar light, as shown in Fig. 7a, which indicated that there were no leaching issues with the Zn-g-C_3N_4 catalyst during the catalytic reaction and the subsequent washing procedures. More significantly, no obvious reduction in conversion or selectivity has been noticed after four consecutive cycles, showing that the Zn-g-C_3N_4 doped catalyst was highly stable for MO degradation.

7. Conclusion

Here, we studied how urea was thermally decomposed to produce Cu, Mn, and Zn-doped g-C_3N_4 composites. Transition metal-doped g-C_3N_4 composites materials exhibited a narrowing bandgap, photo-generated electron-hole pair transfer channel, which is credited to a variety of morphological characteristics and, as a result, increased photocatalytic performance. Through examination of all of the trials' photodegradation activity, it was found that during degradation investigation of synthetic organic MO dye for entire trails, Zn-g-C_3N_4 exhibited higher catalytic efficiency owing to its porous tubular form with higher surface area. The Zn-g-C_3N_4 first-order kinetic constant and optical energy bandgap of 2.49 eV were evaluated, respectively, resulting in enhanced solar energy absorption and higher photocatalytic efficiency for MO. Furthermore, this study determines valuable photocatalysts for decontaminating organic pollutants when irradiated by visible light energy.

CRediT authorship contribution statement

Asif Hussain: Conceptualization, Methodology, Software. **Hamza Naeem, Zaigham Saeed Toor**: Data curation, Writing- Original draft preparation. **M. Umer Farooq, M. Umer**: Visualization, Investigation. **Jianhua Hou, Yuxiong Xue and Xiaozhi Wang**: Supervision, Writing-Reviewing and Editing. **Ji Renlong, Qikai Zhang, M. Hashim**: Software, Validation and Editing. **Samayya Maqsood, M. Boota, Asgar Ali**: Writing- Reviewing and Editing.

Declaration of competing interest

The authors declare that they have no known competing financial interests or personal relationships that could have appeared to influence the work reported in this paper.

Data availability

No data was used for the research described in the article.

Acknowledgements

The authors are grateful for the financial support by the National Natural Science Foundation of China (51602281), Innovative Science and Technology Platform Project of Cooperation between Yangzhou City and Yangzhou University, China (No. YZ202026308), Natural Science Foundation of Shandong Province (No: ZR2019MEM025) Yangzhou University Self-made Experimental Equipment Special Fund (YZUZZ2022-13), Yangzhou University High-end Talent Support Program and the "Qinglan Project" of Jiangsu University.

References

[1] A. Hussain, et al., Fine-tuning internal electric field of BiOBr for suppressed charge recombination, J. Environ. Chem. Eng. 9 (1) (2021) 104766.
[2] A. Hussain, et al., Recent advances in BiOX-based photocatalysts to enhanced efficiency for energy and environment applications, Catal. Rev. (2022) 1–55.
[3] Q. Dou, et al., One-pot synthesis of sodium-doped willow-shaped graphitic carbon nitride for improved photocatalytic activity under visible-light irradiation, J. Colloid Interface Sci. 624 (2022) 79–87.
[4] J. Hou, et al., Fast preparation of oxygen vacancy-rich 2D/2D bismuth oxyhalides-reduced graphene oxide composite with improved visible-light photocatalytic properties by solvent-free grinding, J. Clean. Prod. 328 (2021) 129651.
[5] Z.U. Rehman, et al., Photocatalytic CO2 reduction using TiO2-based photocatalysts and TiO2 Z-scheme heterojunction composites: a review, Molecules 27 (7) (2022) 2069.
[6] T. Zhang, L. Chen, T. Jiang, J. Hou, G. Zhang, A. Hussain, Chemical precipitation synthesis of Bi0.7Fe0.3OCl nanosheets via Fe (III)-doped BiOCl for highly visible light photocatalytic performance, Mater. Today Commun. 26 (2021) 102145.
[7] A. Hussain, et al., Diverse morphological study for nonmetal-doped g-C3N4 composites with narrow bandgap for improved photocatalytic activity, Res. Chem. Intermed. 48 (7) (2022) 2857–2870.
[8] X. Wang, et al., A metal-free polymeric photocatalyst for hydrogen production from water under visible light, Nat. Mater. 8 (1) (2009) 76–80.
[9] J. Jiang, S. Cao, C. Hu, C. Chen, A comparison study of alkali metal-doped g-C3N4 for visible-light photocatalytic hydrogen evolution, Chin. J. Catal. 38 (12) (2017) 1981–1989.
[10] Y.-J. Yuan, F. Wang, B. Hu, H.-W. Lu, Z.-T. Yu, Z. Zou, Significant enhancement in photocatalytic hydrogen evolution from water using a MoS2 nanosheet-coated ZnO heterostructure photocatalyst, Dalton T. 44 (24) (2015) 10997–11003.
[11] K. He, et al., Enhanced visible light photocatalytic H2 production over Z-scheme g-C3N4 nanosheets/WO3 nanorods nanocomposites loaded with Ni (OH) x cocatalysts, Chin. J. Catal. 38 (2) (2017) 240–252.
[12] W.-J. Ong, L.-L. Tan, Y.H. Ng, S.-T. Yong, S.-P.J.C.r. Chai, Graphitic carbon nitride (g-C3N4)-based photocatalysts for artificial photosynthesis and environmental remediation: are we a step closer to achieving sustainability? Chem. Rev. 116 (12) (2016) 7159–7329.
[13] X. Yu, S.F. Ng, L.K. Putri, L.L. Tan, A.R. Mohamed, W. Ong, Point-defect engineering: leveraging imperfections in graphitic carbon nitride (g-C3N4) photocatalysts toward artificial photosynthesis, Small 17 (48) (2021) 2006851.
[14] I. Camussi, et al., g-C3N4-singlet oxygen made easy for organic synthesis: scope and limitations, ACS Sustain. Chem. Eng. 7 (9) (2019) 8176–8182.
[15] Y. Bu, Z. Chen, W. Li, Using electrochemical methods to study the promotion mechanism of the photoelectric conversion performance of Ag-modified mesoporous g-C3N4 heterojunction material, Appl. Catal. B Environ. 144 (2014) 622–630.
[16] G. Dong, et al., The evaluation of super-capacitive performance of novel g-C3N4/PPy nanocomposite electrode material with sandwich-like structure, Compos. Part B-Eng. 162 (2019) 369–377.
[17] R. Monsef, M. Ghiyasiyan-Arani, M. Salavati-Niasari, Design of magnetically recyclable ternary Fe2O3/EuVO4/g-C3N4 nanocomposites for photocatalytic and electrochemical hydrogen storage, ACS Appl. Energy Mater. 4 (1) (2021) 680–695.
[18] X.-L. Zhang, C. Zheng, S.-S. Guo, J. Li, H.-H. Yang, G. Chen, Turn-on fluorescence sensor for intracellular imaging of glutathione using g-C3N4 nanosheet–MnO2 sandwich nanocomposite, Anal. Chem. 86 (7) (2014) 3426–3434.
[19] M. Shakeel, M. Arif, G. Yasin, B. Li, H.D. Khan, Layered by layered Ni-Mn-LDH/g-C3N4 nanohybrid for multi-purpose photo/electrocatalysis: morphology controlled strategy for effective charge carriers separation, Appl. Catal. B Environ. 242 (2019) 485–498.
[20] H. Jiang, Y. Li, D. Wang, X. Hong, B. Liang, Recent advances in heteroatom doped graphitic carbon nitride (g-C3N4) and g-C3N4/metal oxide composite photocatalysts, Curr. Org. Chem. 24 (6) (2020) 673–693.
[21] Z. Wang, Y. Chen, Y. He, W. Jiang, Y. Long, G. Fan, Facile construction of composition-tuned ruthenium-nickel nanoparticles on g-C3N4 for enhanced hydrolysis of ammonia borane without base additives, Int. J. Hydrogen Energ. 46 (21) (2021) 11587–11596.
[22] R. Mohini, N. Lakshminarasimhan, Coupled semiconductor nanocomposite g-C3N4/TiO2 with enhanced visible light photocatalytic activity, Mater. Res. Bull. 76 (2016) 370–375.
[23] Q. Tay, et al., Defect engineered g-C3N4 for efficient visible light photocatalytic hydrogen production, Chem. Mater. 27 (14) (2015) 4930–4933.
[24] J. Hou, et al., Lantern-like bismuth oxyiodide embedded typha-based carbon via in situ self-template and ion exchange–recrystallization for high-performance photocatalysis, Dalton Trans. 47 (19) (2018) 6692–6701.
[25] Y. Che, et al., Bio-inspired Z-scheme g-C3N4/Ag2CrO4 for efficient visible-light photocatalytic hydrogen generation, Sci. Rep. 8 (1) (2018) 1–12.
[26] J. Hou, et al., Defect engineering in polymeric carbon nitride with accordion structure for efficient photocatalytic CO2 reduction and H2 production, Chem. Eng. J. 450 (2022), 138425.
[27] S. Guo, H. Wang, W. Yang, H. Fida, L. You, K. Zhou, Scalable synthesis of ca-doped α-Fe2O3 with abundant oxygen vacancies for enhanced degradation of organic pollutants through peroxymonosulfate activation, Appl. Catal. B Environ. 262 (2020), 118250.
[28] X. Zhao, et al., Simultaneous anchoring of ni nanoparticles and single-atom ni on BCN matrix promotes efficient conversion of nitrate in water into high-value-added ammonia, Chem. Eng. J. 433 (2022), 133190.

[29] J. Wei, F. Li, L. Zhou, D. Han, J. Gong, Strategies for enhancing peroxymonosulfate activation by heterogenous metal-based catalysis: a review, Chin. J. Chem. Eng. 50 (2022) 12–28.
[30] S. Zuo, et al., Polarized heterogeneous CuO-CN for peroxymonosulfate nonradical activation: an enhancement mechanism of mediated electron transfer, Chem. Eng. J. 420 (2021), 127619.
[31] X. She, et al., Template-free synthesis of 2D Porous ultrathin nonmetal-doped g-C3N4 nanosheets with highly efficient photocatalytic H2 evolution from water under visible light, Appl. Catal. B Environ. 187 (2016) 144–153.
[32] L. Jiang, et al., TiO2 nanowires with doped g-C3N4Nanoparticles for enhanced H2 production and photodegradation of pollutants, Nanomaterials 11 (1) (2021) 254.
[33] W. Zhang, et al., Photocatalytic improvement of mn-adsorbed g-C3N4, Appl. Catal. B Environ. 206 (2017) 271–281.
[34] X. Bai, L. Wang, Y. Wang, W. Yao, Y. Zhu, Enhanced oxidation ability of g-C3N4 photocatalyst via C60 modification, Appl. Catal. B Environ. 152 (2014) 262–270.
[35] G. Pan, Z. Sun, Cu-doped g-C3N4 catalyst with stable Cu0 and Cu+ for enhanced amoxicillin degradation by heterogeneous electro-Fenton process at neutral pH, Chemosphere 283 (2021), 131257.
[36] J. Fan, H. Qin, S. Jiang, Mn-doped g-C3N4 composite to activate peroxymonosulfate for acetaminophen degradation: the role of superoxide anion and singlet oxygen, Chem. Eng. J. 359 (2019) 723–732.
[37] A. Hussain, et al., Recent advances in BiOX-based photocatalysts to enhanced efficiency for energy and environment applications, Catal. Rev. (2022) 1–55.
[38] J. Hou, et al., Remarkable cycling durability of lithium-sulfur batteries with interconnected mesoporous hollow carbon nanospheres as high sulfur content host, Chem. Eng. J. 401 (2020), 126141.
[39] C. Chen, et al., Oxygen vacancies induced narrow band gap of BiOCl for efficient visible-light catalytic performance from double radicals, J. Mater. Sci. Technol. 114 (2022) 240–248.
[40] I. El Radaf, H. Al-Zahrani, A.S. Hassanien, Novel synthesis, structural, linear and nonlinear optical properties of p-type kesterite nanosized Cu2MnGeS4 thin films, J. Mater. Sci. Mater. Electron. 31 (11) (2020) 8336–8348.
[41] S. Senol, B. Yalcin, E. Ozugurlu, L. Arda, Structure, microstructure, optical and photocatalytic properties of Mn-doped ZnO nanoparticles, Mater. Res. Express 7 (1) (2020), 015079.
[42] S. Ma, S. Zhan, Y. Xia, P. Wang, Q. Hou, Q. Zhou, Enhanced photocatalytic bactericidal performance and mechanism with novel Ag/ZnO/ g-C3N4 composite under visible light, Catal. Today 330 (2019) 179–188.